Ferroelectric properties and topological polar textures of PbTiO$_3$ from a second-principles open-source interatomic potential

Louis Bastogne [*] and Philippe Ghosez [†]

Theoretical Materials Physics, Q-MAT, Université de Liège, B-4000 Sart-Tilman, Belgium

We report large-scale atomistic simulations of inhomogeneous polar textures in PbTiO$_3$ using a recently developed open-source second-principles effective interatomic potential. The model is meticulously validated against density functional theory, reproducing structural, energetic, and dynamical properties, which ensures predictive reliability beyond the training set. Building on this foundation, we uncover and characterize a rich variety of polar configurations, including Bloch-type domain-wall transition, Ising lines, skyrmions, skyrmioniums, target skyrmions, skyrmion bags in free bulk, as well as antiskyrmions, merons, and antimerons under biaxial tensile strain. These results broaden the known landscape of ferroelectric topologies and highlight PbTiO$_3$ as a versatile host for emergent polar textures with potential applications in functional devices. The open-source model provides the community with a robust and efficient tool for exploring complex ferroelectric phenomena at large scales.

I. INTRODUCTION

Lead titanate (PbTiO$_3$) is a cornerstone material in the ferroelectric community, well known for its large spontaneous polarization [1] and high-temperature ferroelectric-to-paraelectric phase transition [2]. These attributes underpin its widespread use in applications such as transducers and actuators [3]. They also establish PbTiO$_3$ as a prototypical compound for studying fundamental phenomena such as domain formation [4], phase transitions, and piezoelectricity [5].

Over the past decade, several unexpected discoveries in PbTiO$_3$ have significantly advanced our understanding of ferroelectric materials. Notably, distinctive ferroelectric domain walls (DWs) have emerged [6], redefining their role from passive interfaces to active, dynamic entities with novel functionalities such as heat flow regulation [7]. This paradigm shift establishes DWs as key components for enhancing energy efficiency and reducing power consumption in future electronic devices. Another breakthrough was the prediction of polar skyrmions [8], topologically nontrivial solitons analogous to their magnetic counterparts. These skyrmions are stable, electrically controllable, and can exhibit intriguing properties such as chirality and tunable negative capacitance [9–11], positioning them as promising candidates for ultradense data storage and advanced memory technologies [12].

Understanding such complex structures and phenomena requires computational methods that combine high accuracy with scalability. While density functional theory (DFT) offers reliable atomic-scale insights, its computational cost limits its applicability to large systems or long timescales. Second-principles (SP) interatomic potentials [13,14] overcome these constraints by describing the potential energy surface via effective potentials fitted to DFT data [5]. These models have shown predictive capabilities across various studies [8,10,15–20], advancing the exploration, at the atomic scale, of ferroelectric phenomena of technological relevance.

In this work, we introduce an open-source, second-principles effective interatomic potential for PbTiO$_3$, rigorously constructed and meticulously validated against density functional theory data. The model faithfully reproduces structural, energetic, and dynamical properties, including phase transitions, domain-wall energetics, and finite-temperature phonon softening, ensuring its predictive reliability beyond the training set. Building on this foundation, we revisit the landscape of polar textures in PbTiO$_3$. Our simulations not only recover previously reported configurations such as Bloch-type domain walls and skyrmions, but also reveal several other features: the nudged-elastic-band (NEB) pathways for the disappearance of Bloch components and for the collapse of polar skyrmions, the stabilization of skyrmionium and skyrmion bags in bulk PbTiO$_3$, as well as the emergence of meron and antimeron textures, and the equivalence of skyrmion and antiskyrmion states under tensile strain. These results considerably expand the catalog of polar topologies in ferroelectrics and establish PbTiO$_3$ as a versatile platform for emergent polar phenomena. By openly releasing the validated potential, compatible with the open-source MULTIBINIT software [21,22], we also provide the community with a robust and efficient tool to explore complex ferroelectric behaviors at large scales.

II. METHODS

A. First principles

We generated the *ab initio* data for fitting the second-principles interatomic potential using density functional theory calculations with the ABINIT software package [21,22]. We used the generalized gradient approximation (GGA) with

---

[*]Contact author: louis.bastogne@uliege.be

[†]Contact author: philippe.ghosez@uliege.be

the Perdew-Burke-Ernzerhof for solids (PBESol) exchange-correlation functional and a plane-wave-pseudopotential approach, relying on optimized norm-conserving pseudopotentials from the PSEUDODOJO server [23,24]. We treated Pb $5d^{10}6s^26p^2$, Ti $3s^23p^63d^24s^2$, and O $2s^22p^4$ electrons as valence states. We adopted a plane-wave energy cutoff of 65 Ha and used a $8 \times 8 \times 8$ Γ-centered Monkhorst-Pack [25] k-point mesh for the five-atom cubic unit cell, while adapting the k-point sampling to the supercell size in order to maintain a similar high level of convergence. We computed the dynamical matrices for the relaxed cubic $Pm\bar{3}m$ on a $4 \times 4 \times 4$ q-point mesh. From density functional perturbation theory (DFPT) [26], we also extracted essential properties, including the dielectric constant, Born effective charges, strain-phonon coupling, and elastic constants.

B. Second principles

The second-principles model employed in this work is designed to accurately and efficiently describe the Born-Oppenheimer potential energy surface (PES) of crystalline materials. It is based on a Taylor expansion of the PES in terms of structural degrees of freedom and around a reference structure—typically a stationary point where all forces and stresses vanish. This reference can represent a configuration relevant to competing phases or a stable structure suited for analyzing local anharmonicity. The model incorporates all atomic and strain degrees of freedom by systematically distinguishing between harmonic and anharmonic energy contributions. Harmonic interactions, including both short-range forces and long-range dipole-dipole couplings, are derived from DFPT. Anharmonic effects, which capture deviations from harmonic behavior, are introduced through a selection of higher-order terms whose coefficients are fitted to first-principles data, such as energies, forces, and stresses, from a representative set of atomic configurations. Assuming periodic boundary conditions, the model constructs the PES using material-specific parameters. Provided the bond topology remains unchanged, this approach effectively captures the behavior of systems with closely competing structural phases—such as perovskites—where small energy differences drive phase transitions.

We developed the model using the MULTIBINIT [21,22] software package. In practice, the interatomic force constants (IFCs), elastic constants, strain-phonon coupling, Born effective charges, and dielectric constant of the cubic phase $Pm\bar{3}m$ were computed using DFPT calculations from ABINIT [21,22]. A training set of 3644 DFT configurations was used to select and fit the anharmonic coefficients of the model, applying a cutoff radius of $\sqrt{3}/2$ times the cubic lattice parameter to generate symmetry-adapted terms (SATs) up to the eighth order, including strain-phonon coupling and anharmonic elastic constants. We selected 29 SATs via a goal-function (GF) minimization approach and added 66 additional terms to ensure the boundness of the model energy. This automatic bounding procedure, recently developed in the context of MULTIBINIT [21,22], provides a systematic and robust way to stabilize complex models beyond earlier approaches. A more detailed account of these methodological developments will be presented in a forthcoming paper [27].

TABLE I. Structure and energy of various metastable phases of $PbTiO_3$ designated by their space group, as relaxed in DFT. The comparison includes lattice parameters (Å), distortion amplitudes (rotations in degrees and total deformation in Å) with respect to the reference cubic phase, and energy gain ΔE (meV/f.u.) with respect to the five-atom cubic reference structure.

| Phase | Lattice parameter | | | Distortion | | ΔE |
	a (Å)	b (Å)	c (Å)	Rot. (°)	Tot. (Å/f.u)	(meV/f.u.)
$Pm\bar{3}m$	3.917	3.917	3.917	0.0	0.0	0.0
$P4mm$	3.861	3.861	4.244	0.0	0.423	−85.24
$Amm2$	3.886	3.983	3.983	0.0	0.305	−64.00
$R3m$	3.945	3.945	3.945	0.0	0.288	−59.19
$I4/mcm$	3.911	3.911	3.927	4.34	0.105	−3.27
$P4/mbm$	3.915	3.915	3.920	2.09	0.05	−0.23
$Imma$	3.910	3.919	3.919	3.22	0.111	−3.63
$R\bar{3}c$	3.916	3.916	3.916	2.63	0.110	−3.66

Finite-temperature simulations were performed using a hybrid molecular dynamics–Monte Carlo (HMC) scheme [28,29], as implemented in ABINIT [21,22]. Each HMC sweep consisted of 40 molecular dynamics steps with a time step of 0.72 fs, performed in the NPT ensemble. After 500 sweeps for thermalization, simulations typically included 2000 HMC sweeps, increased to 4000 in the vicinity of phase transitions. Structural relaxations used the Broyden-Fletcher-Goldfarb-Shanno (BFGS) algorithm in ABINIT [21,22], and energy barriers were explored using the nudged elastic band (NEB) method with the Quick-Min algorithm [30,31]. Phonon dispersions at 0 K were obtained with the SP potential in ABINIT [21,22], while finite-temperature phonons were calculated using TDEP software [32]. This atomistic model has been successfully applied in previous studies [16,20,33,52].

III. SECOND-PRINCIPLES MODEL

A. Training set and model construction

We built the training set (TS) used to fit our second-principles model with the same successful approach used for other compounds such as the prototypical ferroelectric $BaTiO_3$ [18], nonpolar $SrTiO_3$, and antiferroelectric $PbZrO_3$ [34]. By analyzing the phonon-dispersion curve, we first identify unstable modes at the Γ, M, and R points, which align with a $2 \times 2 \times 2$ supercell of the $Pm\bar{3}m$ phase. Condensing then all possible combinations of these unstable modes, we identify six (meta)stable phases, summarized in Table I. These results match closely with previous studies [35].

Starting from this information, we build the TS making a smart sampling of configuration space. We explore the PES following linear interpolation paths between all pairs of relaxed phases. Additionally, to capture thermal effects, we add thermal noise to selected configurations by populating phonons from the reference structure [36], adjusting the amplitude to ensure that the total energy lies between the energy of the ground state and up to twice that energy above the reference structure. This initial model is then refined: after fitting a preliminary model, we run molecular dynamics simulations at various temperatures using this preliminary model, generating
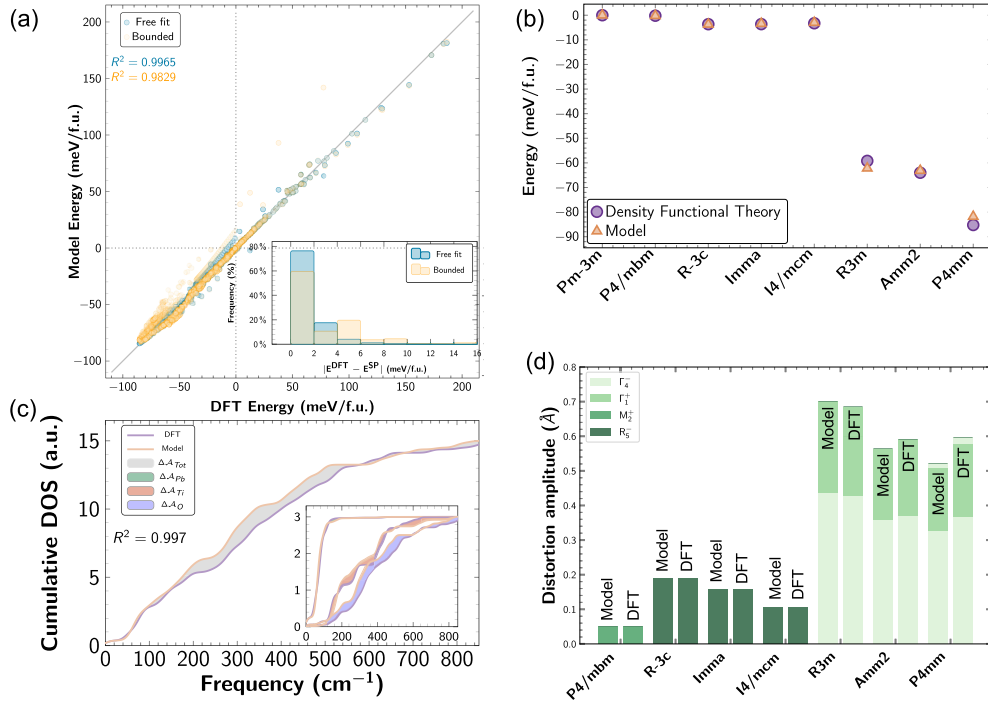
FIG. 1. Validation against DFT of the interatomic potential for $PbTiO_3$. (a) Comparison between model and DFT energies, as predicted for the structures contained in the training set. The inset shows the distribution of the amplitude of absolute error made by the model. (b) Comparison between DFT and model energies for different (meta)stable phases, as consistently relaxed within each approach. (c) Comparison between DFT and model cumulative total phonon density of states in the tetragonal $P4mm$ ground state. The inset shows the comparison between DFT and model contributions to the cumulative phonon density of states individually for each type of atom. (d) Comparison between DFT and model distortion amplitudes for different meta- and stable phases, as consistently relaxed within each approach.

additional data to feed and improve the accuracy of the final model. Combining all data, we end up with a training set that contains 3644 configurations. With these configurations, we have sampled the PES of $PbTiO_3$ around the cubic reference structure, allowing us to fit a final model ready for the validation steps.

B. Validation

We first validate our second-principles model by testing its ability to reproduce the data of the training set. As shown in Fig. 1(a), our free fit model achieves a good fit quality with $R^2 > 0.996$. The free fit is obtained without any constraint. However, our model consists of a truncated polynomial expansion of the energy around a reference structure. This expansion is often not bounded from below, meaning that the energy can eventually diverge when increasing some displacements of the atoms compared to the reference structure. To address this problem, we performed an automatic bounding of our model by adding higher-order even terms associated with a positive coefficient. As shown in Fig. 1(a), the bounded model maintains the accuracy of the fit ($R^2 > 0.982$) while, at the same time, eliminating the possible divergence of the model.

In order to go one step further in the validation of our model, we performed structural relaxations and compared all stationary phases identified in Fig. 1(b). As shown in Figs. 1(b) and 1(c), not only the energies but also the structural distortion obtained from the model-based structural

relaxations are highly consistent with the results obtained from the first-principles relaxations. Indeed, the largest error (0.68 meV/atom for the ground state) is within the typical convergence criterion for DFT calculations. Moreover, the biggest difference with respect to the total distortion is equal to 0.049 Å/f.u., which is negligible when considering the complexity of the system.

Finally, we computed the cumulated density of states of the phonon-dispersion curves in the $P4mm$ phase at 0 K using DFPT and our model [see Fig. 1(c)]. To compare them, we calculate the difference of area, $\Delta\mathcal{A}$, between the two cumulative density of states (DOS) and normalize it with respect to the DFT result. Then, we obtain a quality factor $\Delta a = 1 - \Delta\mathcal{A}/\mathcal{A}_{DFT} = 0.95$ that reflects the quality of our model to reproduce the phonon in this ground-state phase. Looking at the cumulated DOS atom by atom, we can attribute the main discrepancy to the oxygen atoms.

Comparison of the model with an independent DFT test set is also reported in the attached model validation passport [37]. All together, these results demonstrate that our model can accurately capture not only the PES, but also the fine structural details of the system, reinforcing its predictive capability.

IV. RESULTS

A. Finite-temperature ferroelectric transition

Once the model has been validated, all the advantages of the SP approach can be harnessed, such as large-scale finite-temperature simulations. The first natural finite-temperature
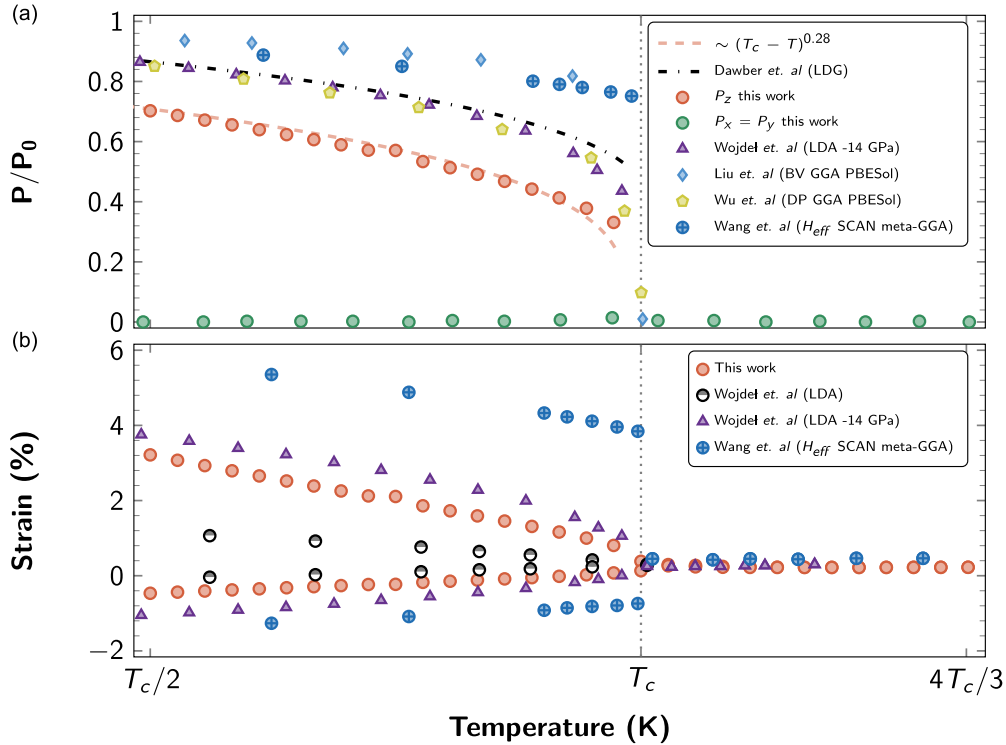
FIG. 2. Ferroelectric *P4mm* to paraelectric *Pm$\bar{3}$m* phase transition of PbTiO$_3$ in temperature as predicted by the interatomic potential. (a) Evolution of the spontaneous polarization (normalized with the polarization P_0 at 0 K) with temperature, in comparison with the results of Refs. [13,38–41]. The orange dashed curve shows a critical exponent fit of $n = 0.28$. (b) Evolution of the homogeneous strains with temperature, in comparison with the results of Refs. [13,46]. Note that the data of Ref. [13] with a negative pressure of -14 GPa have been shifted to align with our strain at T_c.

simulation to perform concerns the well-known ferroelectric-to-paraelectric phase transition. As shown in Fig. 2, our model captures the first-order nature of the phase transition, but predicts it to occur at 400 K, which is significantly lower than the experimentally observed transition temperature of 760 K [2].

Figure 2(a) depicts the evolution of the spontaneous polarization P/P_0 as a function of temperature, where P_0 is the polarization at 0 K. Our results are compared with theoretical predictions from previous theoretical methods fitted on various data [13,38–41]. The polarization decreases with increasing temperature, dropping sharply near the transition temperature, consistent with the first-order character of the transition. We notice that the polarization P_0 of our model in Fig. 2(a) has been estimated using the Born effective charge of the cubic phase yielding to a slightly overestimated value of 1.1 C/m^2. Using instead the Born effective charge of the *P4mm* phase would give an underestimated value of 0.84 C/m^2. The more accurate P_0 calculated for the same structure in DFT using the Berry phase is 0.99 C/m^2, which is in good agreement with previous calculations [42].

Figure 2(b) shows the strain evolution with temperature, highlighting the structural changes accompanying the phase transition. The strain exhibits a discontinuity at T_c, further confirming the first-order nature of the transition. Our results are in good agreement with Local-Density Approximation (LDA)-based calculations under negative pressure (-14 GPa).

The underestimation of T_c is typical feature of second-principles models, which is often attributed to the inherent

limitations in the underlying exchange-correlation functionals [43–45] on which the model is fitted. Moreover, here, the high-order development of the model up to order eight combined with the bounding process makes the model stiffer and could contribute to explain the underestimation of the critical temperature of the model. Finally, let us note that the T_c of our model lies between the values obtained from LDA-based second-principles [13] and machine-learning meta-GGA methods [46], which, respectively, under- and overestimate T_c (and, by extension, also c/a or P) in the absence of external pressure. Their closer agreement is only achieved under pressure correction, which our model does not require. Although a weakness, the under- or overestimation of the critical temperature does not necessarily prevent the practical application of a model and can be handled from simple temperature renormalization, as used in the next section.

B. Temperature-dependent phonon properties

Since PbTiO$_3$ is known to show a displacive character [47], it is interesting to simulate how the phonon-dispersion curves are evolving with temperature. For each simulated temperature $T_{\text{sim}} = (T_{c,\text{sim}}/T_{c,\text{exp}})T_{\text{exp}}$, we performed a NPT simulation followed by a NVT simulation considering the average volume of the previous simulation. We extract a temperature-dependent dynamical matrix from molecular dynamics and then obtain temperature-dependent phonon-dispersion curves. As shown in Fig. 3(a), above $T_{c,\text{sim}}$, the system is stable in the cubic phase and no unstable phonons have been found. Moreover, a polar mode at Γ point is softening from 81 to
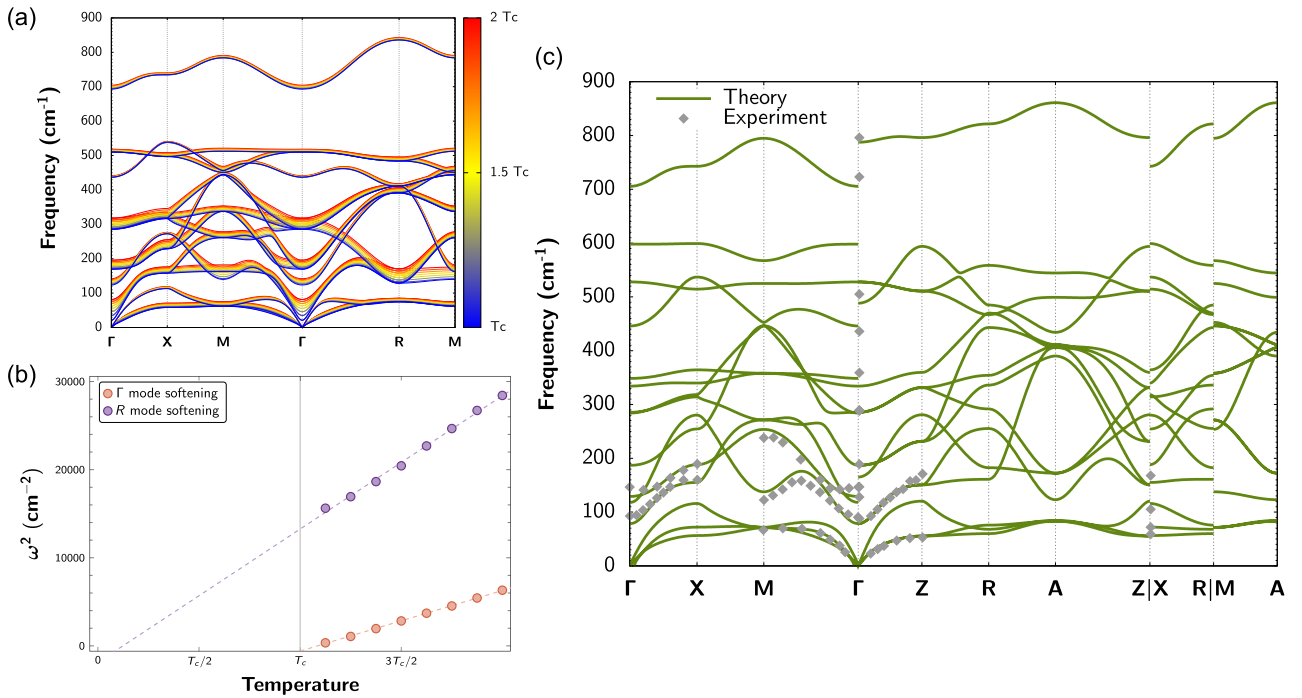
FIG. 3. Temperature-dependent phonon-dispersion curves of $PbTiO_3$. (a) Temperature-dependent phonon dispersion in the cubic phase above T_c (T_c stands for critical temperature of the simulation considering $4 \times 4 \times 4$ supercell). (b) Mode softenings at Γ (polar modes) and R (antiferrodistortive modes). (c) Temperature-dependent phonon-dispersion curves in the tetragonal phase at $T_{exp} = 300$ K in a $4 \times 4 \times 4$ supercell, compared with experimental data from Refs. [49,50].

21 cm^{-1} when decreasing the temperature from $2\,T_{c,\mathrm{sim}}$ to $T_{c,\mathrm{sim}}$. Interestingly, other modes are softening at different places throughout the Brillouin zone, in particular at R and M. These antiferrodistortive modes relate to out-of phase $(-)$ and in-phase $(+)$ rotation of the oxygen octahedra.

As illustrated in Fig. 3(b), ω^2 evolve linearly with temperature, in fair agreement with the soft mode theory of Cochran [48]. This simultaneous softening at the center and the border of the Brillouin zone is the signature of typical competition between oxygen octahedra rotations and polar distortions in materials with a Goldschmidt tolerance factor close to one, such as $PbTiO_3$ and $SrTiO_3$. In the case of $PbTiO_3$, the polar modes are softening faster than the oxygen octahedra rotations, leading to a polar phase transition when the temperature is decreasing, in contrast to the scenario occurring in $SrTiO_3$.

Since our model can predict the temperature-dependent phonon-dispersion curve, we can use it to investigate phonons at room temperature ($T_{exp} = 300$ K) and compare it with experiment. As shown in Fig. 3(c), our model shows excellent agreement with the experimental data, as demonstrated by the close correspondence between the calculated frequencies and the measured frequencies [49,50] over a wide frequency range and between different paths connecting points of high symmetry in the Brillouin zone. This strong concordance highlights the accuracy and reliability of our theoretical predictions in capturing the vibrational properties of the material, despite the underestimation of the critical temperature.

C. Structure and energetics of ferroelectric domain walls

Domain walls are extended defects that separate homogeneous regions (domains) with distinct orientations of an order parameter. They represent transitional areas where the order parameter must rotate or vanish, often carrying intrinsic properties that differ significantly from those inside the domains they connect. In tetragonal $PbTiO_3$, many studies have focused on 180° and 90° ferroelectric domain walls [4,51]. The 180° walls separate domains of opposite polarizations, while 90° walls separate domains with orthogonal polarization directions.

Ferroelectric DWs are classified according to the way the polarization evolves from one domain to the other. If the polarization remains along the same axis and switches by changing its magnitude, the wall is called an Ising wall. In contrast, walls exhibiting a smooth rotation of the polarization within the plane of the wall are called Bloch walls, while those involving a rotation perpendicular to the wall plane are called Néel walls. Originally, DWs in $PbTiO_3$ were considered as Ising walls [4]. More recently, however, Wojdeł and Íñiguez [6] proposed that 180° DWs can also develop, confined inside the wall itself, an additional ferroelectric component. Since the latter is oriented perpendicular to the domain polarization, such walls are often called Bloch walls.

Our computations of 180° DWs structures and energies concern stripe domain configurations in which the domain polarization is oriented along x, the domain wall is Pb centered (confirmed here to be the most stable location [4]) and oriented in the xy plane, and each domain has a width $t = 10$ u.c. along z ($1 \times 1 \times 20$ simulation box). During the computation, the atomic structure is fully optimized, including simultaneous relaxations of cell parameters and internal degrees of freedom. As explained in Ref. [52], atomic relaxations can take place along the x, y, and z directions, giving rise to

TABLE II. Comparison of DW energies (mJ/m^2) and maximal component of polarization (μC/cm^2) for a 180° Pb-centered stripe configuration with a domain width of 10 u.c. ($1 \times 1 \times 20$ u.c. simulation box) and for a 90° O-O centered with a domain width of 4 u.c. ($1 \times 1 \times 8$ u.c. simulation box). The parentheses are the comparison with Ref. [52] for 180° and Ref. [4] for 90°.

Type	E^{DW}	P_x	P_y	P_z
Constraint 180° Ising	206 (196)	93 (102)	0.0 (0.0)	0.0 (0.0)
Fully relaxed 180° Ising	201 (191)	93 (102)	0.0 (0.0)	0.15 (0.37)
Fully relaxed 180° Bloch	195 (187)	93 (101)	36 (36)	0.17 (0.33)
Fixed cell parameters 90°	39 (32.5)	67	42	3×10^{-4}

polarization components that can be labeled, respectively, as Ising, Bloch, and Néel. Due to the symmetry breaking produced by the DW, full relaxation of so-called Ising walls typically also naturally includes small atomic relaxations along z (Néel type) [53], while, due to its ferroelectric nature, the Bloch component can be present or not. Hereafter, following the previous literature, we call "(relaxed) Ising walls" those including both Ising and Néel types of relaxations, while we refer to those artificially restricted to Ising-type relaxation as "constrained Ising walls". We then call Bloch walls those additionally developing a Bloch polarization component along y.

As discussed in Ref. [52], in stripe configurations, the DW structure and energy only slowly converge with the domain-wall density (i.e., $1/t$) and the values reported here are therefore specific to $t = 10$ u.c. For 180° Ising walls (constrained and relaxed), the DW energies of the model are comparable to DFT values (Table II). Also the cell parameters and Bloch and Néel components of the polarization are closely reproduced. As shown in Table II, the Néel component P_z is much smaller than the Ising and Bloch components, as it originates solely from the strain gradient induced by the domain wall. Nevertheless, despite the small magnitude of P_z, the energy gain associated to the atomic relaxation along z is comparable to the energy difference between the fully relaxed Ising and Bloch configurations.

For 90° Ising walls, we followed the same setup as in Ref. [4]. Table II shows good agreement between the domain-wall energy given by our model and that reported in Ref. [4].

Since our model is validated on conventional Ising 180° and 90° domain walls, it can now be confidently applied to explore less conventional configurations such as Bloch walls. Figure 4(a) presents a striking confirmation of our model's ability to capture the fundamental properties of 180° domain walls (DWs) in PbTiO$_3$ with an additional ferroelectric Bloch component, confined at the domain wall. Specifically, and without having been explicitly trained on such inhomogeneous configurations, it predicts a ferroelectric component within the DW, with a polarization of $P_y = 36$ μC/cm^2 (36 μC/cm^2 in DFT), in excellent agreement with previous DFT-based theoretical findings [6,52,54] and in much better agreement than the new generation of effective Hamiltonians [55]. Moreover, our calculations reveal an energy difference of approximately 6 meV/□ between Ising and Bloch DW configurations (for a $1 \times 1 \times 20$ supercell, where meV/□ denotes the energy per unit-cell surface area of the DW). This result is in good agreement with DFT (see Table II), with the energy difference for the whole supercell from DFT and our model differing by 3.8 meV per formula unit. The robustness of our

model is further reinforced by its accurate reproduction of the ferroelectric behavior of the Bloch component: the energy of the Bloch DW remains unchanged regardless of whether the Bloch components are aligned or antialigned. These results confirm the deep-seated connection between ferroelectricity and topological structures in PbTiO$_3$, strengthening its role as a cornerstone material for advanced electronics and data storage. The discovery of ferroelectric Bloch-type components confined within DWs [6] has revolutionized the field by highlighting their potential in the design of polar skyrmions [8] and other emerging topological configurations [56,57]. Given its extensive range of DW configurations and strong ferroelectric properties [4,51,58], PbTiO$_3$ continues to be a prime candidate for exploring the interplay between ferroelectricity and topology. Accurately modeling these intricate behaviors is crucial for pushing the frontiers of ferroelectric research and unlocking novel functionalities for future technologies.

To investigate the mechanism by which domain structures with domain walls (DWs) transition to a monodomain state, we performed nudged elastic band (NEB) calculations. This method allows us to systematically determine the minimum-energy path for the transition from a configuration with domains to a monodomain state, shedding light on the energetic barriers and intermediate configurations involved in stabilizing a monodomain phase. A key aspect of this transition is that there are two possible monodomain states: one aligned with the domain and another aligned with the DW in the case of Bloch walls. Understanding this process is crucial for predicting how an applied electric field—whether aligned with the polarization in the domain or the DW—will drive the system from a domain structure to a monodomain state. Additionally, this transition provides insight into how DWs vanish with increasing temperature. Figure 4(b) presents the NEB calculations performed with our model, showing the predicted transition paths.

The pathway from a Bloch DW to a monodomain with polarization aligned with one of the original domains involves a DW displacement followed by DW annihilation, leading to several local minima and a rise in energy as the DWs approach each other. Interestingly, the last local minimum arises when the DWs are separated by three unit cells. After that, the DWs are too close to each other and the system evolves continuously to a monodomain state.

In contrast, the transition from a Bloch DW to a monodomain with the polarization aligned with the Bloch component of the DW follows a smooth rotation of the domain. Both transitions exhibit comparable energy barriers, which are significantly higher than that of the Bloch-to-Ising transition. This suggests that with increasing temperature, the
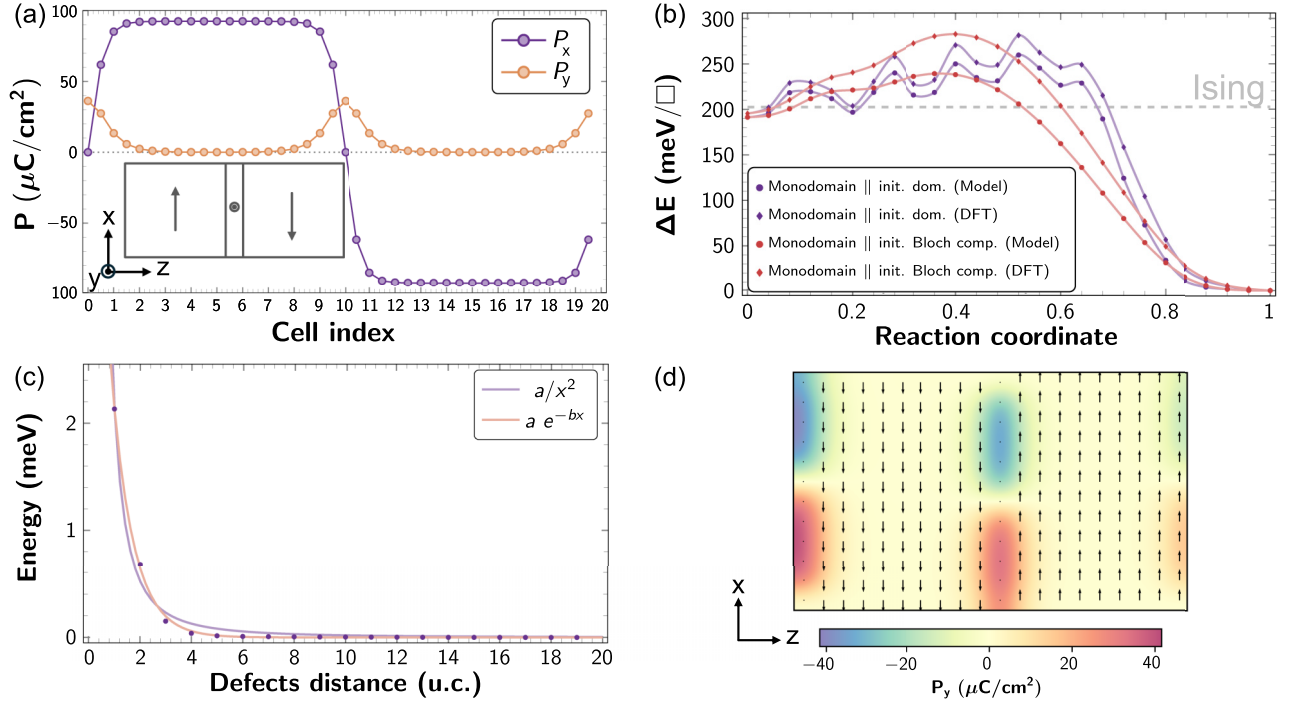
FIG. 4. Characterization of 180° Bloch DW in tetragonal PbTiO$_3$. (a) Polarization profile of $P \parallel [100]$ (P_x) (purple) and $P \parallel [010]$ (P_y) (orange) in a 180° domain structure. (b) Results of NEB calculations illustrating the domain-wall energy evolution along the transition from a Bloch DW to two distinct monodomain configurations: one with the final polarization aligned parallel to the original domain polarization and the other with the final polarization oriented perpendicular to the original domain polarization. Both NEB paths are compared to DFT calculations. (c) Evolution of the energy when DWs approach each other and its fit with exponential and power laws. (d) Polarization profile in *x-z* plane highlighting the appearance of Ising lines within the DW.

material will first undergo a Bloch-to-Ising transition before complete suppression of the DW, consistent with previous findings [6]. Figure 4(b) also illustrates that our model effectively captures the energetics of the Bloch DW configuration compared to DFT and reproduces the energy path of transition to the monodomain.

Furthermore, we investigated how the DWs interact [see Fig. 4(c)] as they approach each other. Significant DW interactions begin when they are less than three unit cells apart, and their strength increases exponentially as they move closer, which is in good agreement with the NEB calculation previously discussed. The interaction is following an approximate trend of $\sim 6.3e^{-1.1x}$, where x is the distance between DWs. For comparison, a fitted power law of the type $2.1/x^{1.8}$ appears less appropriate. The exponential decay observed here reflects the short-range interactions between adjacent domain walls. This fast decay contrasts with the more slowly converging behavior (power law) observed in terms of domain-wall density, which is governed by long-range elastic relaxations; see Ref. [52].

Beyond four unit cells, DWs do not significantly interact, which may lead to disorder of the Bloch component as the temperature rises, complicating its detection. This is due to the ferroelectric nature of the DW, meaning that the relative orientation between two DWs is no longer important beyond four unit cells. This transition behavior highlights the versatility of our model in capturing complex domain dynamics and the intricate energy landscapes of PbTiO$_3$.

To deepen our understanding of DW structures, we examine potential disorders that may arise within them, focusing on the stabilization of Ising lines, as proposed in BaTiO$_3$ [59]. Figure 4(d) shows that the relaxed structure inside the 180° DW of PbTiO$_3$ closely resembles the configuration predicted by Stepkova *et al.* for 180° Bloch DWs in BaTiO$_3$ [60] and observed experimentally in LiTaO$_3$ [61]. In our case, the Ising lines configuration is 2.95 meV/□ higher than the aligned Bloch configuration. Here we report Ising lines in PbTiO$_3$, which calls for experimental verification. Independently, this also highlights the challenge of detecting Bloch components using experimental techniques such as x-ray diffraction (XRD), which require a well-ordered Bloch component for accurate observation [33].

D. Stabilization of polar skyrmionic textures

Since our model naturally reproduces the Bloch DW, which forms the fundamental structure of the Bloch skyrmion in PbTiO$_3$, it is natural that we can stabilize this configuration. Skyrmions are topological textures characterized by a rotation of an internal order parameter (spin, polarization), forming vortexlike structures with a well-defined topological charge. They emerge as stable or metastable configurations in systems where competing interactions or boundary conditions give rise to nontrivial winding patterns. Figure 5 shows the stabilization of a polar Bloch skyrmion using our model, following the procedure described in Ref. [8]. The
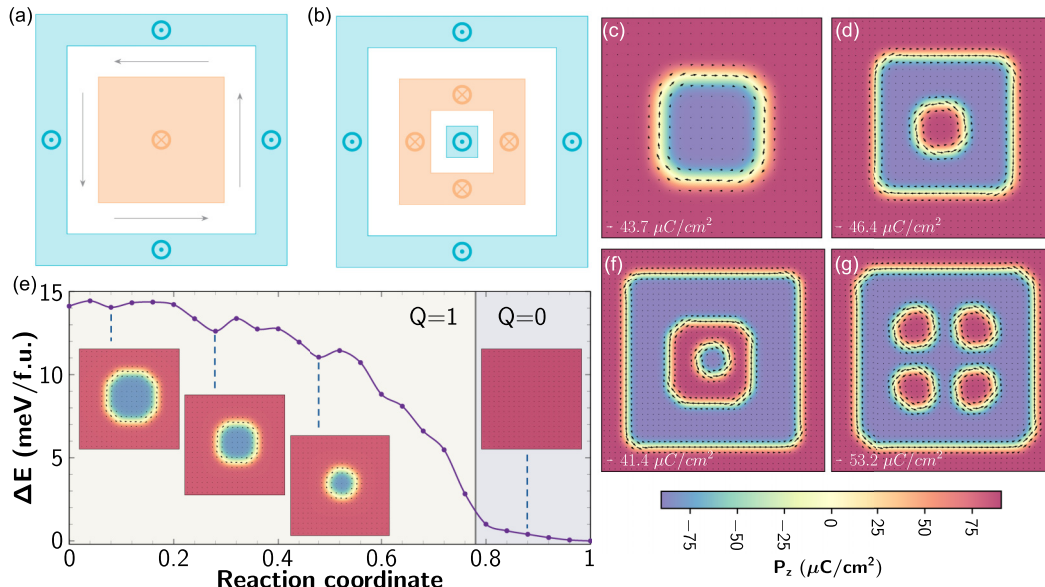
FIG. 5. Skyrmion, skyrmionium, target-skyrmion, and skyrmion bag in PbTiO$_3$. (a) Sketch of a Bloch skyrmion. (b) Sketch of a skyrmionium constructed using 180° domains. (c) Relaxed Bloch skyrmion using a $20 \times 20 \times 1$ supercell, starting from the configuration of (a). (d) Relaxed Bloch skyrmionium using a $32 \times 32 \times 1$ supercell, starting from the configuration of (b). (e) Results of a NEB calculation along the path between the skyrmion and monodomain states using a $20 \times 20 \times 1$ supercell. (f) Relaxed Bloch target-skyrmion using a $41 \times 41 \times 1$ supercell. (g) Relaxed Bloch skyrmion bag using a $40 \times 40 \times 1$ supercell.

polarization profile exhibits a tightly bound, vortexlike arrangement, with polarization components forming close patterns around a central core that is polarized in the opposite direction of the surrounding matrix. Different recent theoretical studies further demonstrated that acoustic phonon excitation (APEX) [16] or an inhomogeneous electric field [20] can dynamically stabilize such skyrmions, allowing controlled creation and manipulation of these topological structures.

To analyze the transition from a skyrmion to a monodomain state, we perform a NEB calculation. Figure 5(e) illustrates the minimum-energy pathway, where the skyrmion progressively shrinks while transforming into a monodomain structure. Along this pathway, several intermediate configurations are observed, some of which correspond to metastable states with distinct local energy minima. This finding agrees with finite-temperature simulations. Indeed, the skyrmion remains stable up to 50 K in a $20 \times 20 \times 4$ supercell. Beyond this temperature, thermal effects induce its collapse into a monodomain state through a pinning-depinning transition. This behavior aligns with the observations of Liu *et al.* in Ref. [62].

In addition, the last minimum exhibited by the NEB calculation corresponds to a skyrmion radius of four unit cells, which is consistent with the domain-wall interaction length discussed in the previous section.

Given the robustness of our model in reproducing topologies reported in the literature, we extend our study to explore additional polar textures.

Figure 5(d) shows a Bloch-type skyrmionium stabilized in PbTiO$_3$. A "skyrmionium" is a complex polar texture characterized by concentric polarization domains. In this configuration, the central core of a given polarization is encircled by a ring of opposite polarization, forming a nontrivial polar

structure with net zero topological charge. Analogous textures have been previously reported in ferromagnetic systems under various names, including "2π-vortex" [63,64] and "donut skyrmion" [65]; the term skyrmionium is usually given to a skyrmion surrounded by a domain wall of opposite topological charge [66] and it is the convention we are adopting here. In magnetic systems, the relatively simple stabilization of skyrmioniums has made them promising candidates for nonvolatile memory applications [67].

The term "target-skyrmion" [68] is also sometimes used for such structures but, rigorously speaking, target-skyrmion more precisely refers to multiring textures with nonzero topological charge. In our vocabulary, the target-skyrmion so consists of multiple concentric polarization domains, giving rise to a nonzero topological charge. They were also successfully stabilized in PbTiO$_3$, as illustrated in Fig. 5(d).

Finally "skyrmion bags" are also sometimes reported in magnetic systems [68,69]. They consist of several skyrmion-like cores confined within a larger enclosing domain wall, resulting in a composite texture with higher total topological charge. They can also be stabilized in PbTiO$_3$, as illustrated in Fig. 5(f).

Figure 5 highlights the rich diversity of topological structures accessible in ferroelectrics and points to new possibilities for information encoding based on topological textures. These structures can be understood within a unified $k\pi$-skyrmion framework, where the out-of-plane polarization component reverses k times between the center and the periphery. Within this scheme, the standard skyrmion, skyrmionium, and target-skyrmion correspond to $k = 1$, $k = 2$, and $k = 3$, respectively, reflecting increasing radial complexity and domain-wall multiplicity [63].

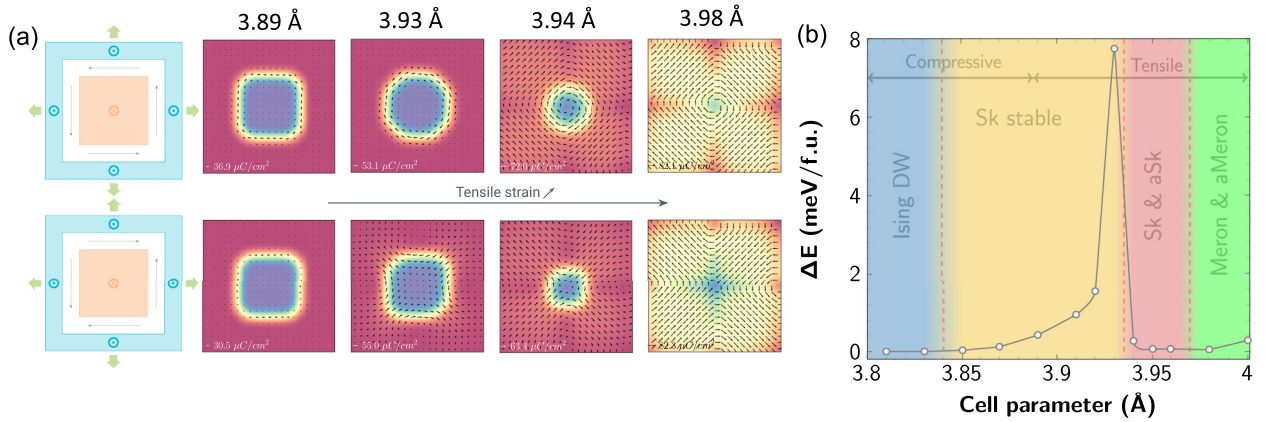In our case, these textures are stabilized by selectively reversing the P_z component within the skyrmion core. By

FIG. 6. Effect of biaxial strain on the stability of skyrmion and antiskyrmion in PbTiO$_3$. (a) Sketch of the initial configuration of a skyrmion and an antiskyrmion and the evolution of the relaxed polar texture of skyrmion and antiskyrmion under biaxial strain. (b) Evolution of the difference of energy between skyrmion and antiskyrmion for various values of in-plane cell parameters ($\Delta E = E_{aSk} - E_{Sk}$).

controlling the number and spatial arrangement of these reversals, we can, in principle, realize $k\pi$-skyrmions with arbitrary values of k, constrained only by the physical size of the system and the spatial resolution of the applied electric field.

While skyrmionium textures have been observed in PbTiO$_3$/SrTiO$_3$ superlattices, where interfacial coupling facilitates their formation [70,71], our results demonstrate that a broader variety of topological structures can also be stabilized in bulk PbTiO$_3$. This has been achieved here by intentionally imposing a guess atomic structure for the distinct textures and subsequently relaxing the original configuration, but we have checked that these various textures can also be stabilized via the activation of an appropriate localized Gaussian electric field, as proposed in Ref. [20], which further opens the way to their dynamical manipulation.

E. Influence of biaxial strain on topological defects

An antiskyrmion is a topological texture characterized by a vorticity opposite to that of a skyrmion. It typically involves an inverted internal configuration. Skyrmions exhibit a characteristic rotational sense—clockwise or counterclockwise. In contrast, antiskyrmions display the opposite winding. The skyrmions discussed earlier emerge from the Bloch component of the DW. An antiskyrmion can thus be constructed by reversing the internal structure of this component, as shown in Fig. 6(a). This approach is justified by the ferroelectric nature of the Bloch component.

In the absence of strain constraints, the skyrmion is more stable than the antiskyrmion, as shown in Fig. 6(b). The antiskyrmion is not stable at finite temperature. Indeed, it transforms into a skyrmion even at low temperatures. Under epitaxial tensile strain, the energy difference between the skyrmion and the antiskyrmion increases, as shown in Fig. 6(b). This is due to the enhancement of the in-plane component under tensile strain. It increases the energetic cost of the head-to-head configuration in the antiskyrmion. However, at a critical threshold (around 3.94 Å), the energy difference abruptly drops to zero. This effect is analogous to the recent

theoretical prediction of [001]$_{pc}$ skyrmions and antiskyrmions in the rhombohedral R3m phase of BaTiO$_3$ and KNbO$_3$ [19].

For cell parameters above 3.94 Å, the in-plane component extends throughout the supercell. As a result, skyrmions and antiskyrmions become energetically degenerate. This is due to periodic boundary conditions and the Poincaré-Hopf theorem [72], which dictates that the total vorticity in the simulation cell must vanish. As a result, vortex and antivortex textures must cancel each other. It is worth noting that the predicted skyrmion structures in BaTiO$_3$, KNbO$_3$, and those generated by our model closely resemble the skyrmions previously reported in PbTiO$_3$ under tensile strain [8], although antiskyrmions have not yet been observed in PbTiO$_3$ to date. Finally, Fig. 6(b) also shows that at high compressive epitaxial strain, the energy difference between skyrmions and antiskyrmions tends toward zero.

At high compressive strain, the Bloch component diminishes so that both skyrmion and antiskyrmion textures approach a similar Ising-type domain wall. At high tensile strain, the out-of-plane component localizes at the vortex and antivortex cores. This transforms skyrmions and antiskyrmions into merons and antimerons. Interestingly, Gómez-Ortiz et al. [19] also demonstrated that skyrmions and antiskyrmions can be stabilized through the application of a spatially modulated electric field [19]. A similar approach could be envisioned here to stabilize skyrmions and antiskyrmions, but also merons and antimerons.

In this section, we have shown that our model effectively captures the formation, stability, and transformation of defects in PbTiO$_3$, including DWs, skyrmions, antiskyrmion, meron, antimeron, and skyrmionium. This capability offers a comprehensive understanding of defect dynamics and reinforces the model's reliability in representing complex ferroelectric behavior. These achievements not only expand the known polar topologies in PbTiO$_3$, but also highlight its potential for hosting diverse topological structures under strain.

V. CONCLUSIONS

We have developed a second-principles effective interatomic potential for PbTiO$_3$ that successfully reproduces

critical physical phenomena, including phase transitions, temperature-dependent phonon behavior, and complex DW dynamics and also allows the discovery of new polar textures in $PbTiO_3$ such as Ising lines, skyrmionium, target-skyrmion, skyrmion bag, antiskyrmion, meron, and antimeron. By providing a genuinely open-source, user-friendly implementation compatible with MULTIBINIT [21,22], we aim to bridge the gap between small-scale DFT calculations and large-scale simulations essential for practical applications. This work aligns with the principles of open science, ensuring that the model is accessible and reproducible, thereby encouraging collaboration and innovation in the study of ferroelectric materials. We hope this contribution serves as a foundation for further advances in materials research, fostering a transparent and cooperative scientific community.

ACKNOWLEDGMENTS

DATA AVAILABILITY

The second-principles MULTIBINIT model is open source and available at Ref. [37], along with a validation assessment. Other supporting data are available from the authors upon reasonable request.

[1] R. J. Nelmes and W. F. Kuhs, The crystal structure of tetragonal $PbTiO_3$ at room temperature and at 700 K, Solid State Commun. **54**, 721 (1985).

[2] G. Shirane and S. Hoshino, On the phase transition in lead titanate, J. Phys. Soc. Jpn. **6**, 265 (1951).

[3] S. Zhang, F. Li, J. Luo, R. Sahul, and T. R. Shrout, Relaxor-$PbTiO_3$ single crystals for various applications, IEEE Trans. Ultrason., Ferroelect., Freq. Contr. **60**, 1572 (2013).

[4] B. Meyer and D. Vanderbilt, *Ab initio* study of ferroelectric domain walls in $PbTiO_3$, Phys. Rev. B **65**, 104111 (2002).

[5] P. Ghosez and J. Junquera, Modeling of ferroelectric oxide perovskites: From first to second principles, Annu. Rev. Condens. Matter Phys. **13**, 325 (2022).

[6] J. C. Wojdeł and J. Iniguez, Ferroelectric transitions at ferroelectric domain walls found from first principles, Phys. Rev. Lett. **112**, 247603 (2014).

[7] E. Langenberg, D. Saha, M. E. Holtz, J.-J. Wang, D. Bugallo, E. Ferreiro-Vila, H. Paik, I. Hanke, S. Ganschow, D. A. Muller *et al.*, Ferroelectric domain walls in $PbTiO_3$ are effective regulators of heat flow at room temperature, Nano Lett. **19**, 7901 (2019).

[8] M. A. Pereira Gonçalves, C. Escorihuela-Sayalero, P. Garca-Fernández, J. Junquera, and J. Íñiguez, Theoretical guidelines to create and tune electric skyrmion bubbles, Sci. Adv. **5**, eaau7023 (2019).

[9] Y. Tikhonov, S. Kondovych, J. Mangeri, M. Pavlenko, L. Baudry, A. Sené, A. Galda, S. Nakhmanson, O. Heinonen, A. Razumnaya *et al.*, Controllable skyrmion chirality in ferroelectrics, Sci. Rep. **10**, 8657 (2020).

[10] P. Zubko, J. C. Wojdeł, M. Hadjimichael, S. Fernandez-Pena, A. Sené, I. Luk'yanchuk, J.-M. Triscone, and J. Íñiguez, Negative capacitance in multidomain ferroelectric superlattices, Nature (London) **534**, 524 (2016).

[11] C. Guo, S. Tang, D. Liang, J. Wang, and H. Huang, Continuously tuning negative capacitance via field-driven polar skyrmions in ferroelectric trilayer wrinkled films, ACS Nano **19**, 8085 (2025).

[12] G. Du, L. Zhou, Y. Huang, Y. Wu, H. Tian, and Z. Hong, Design of polar skyrmion-based nanoelectronic prototype devices with phase-field simulations, Adv. Funct. Mater. **34**, 2405594 (2024).

[13] J. C. Wojdeł, P. Hermet, M. P. Ljungberg, P. Ghosez, and J. Iniguez, First-principles model potentials for lattice-dynamical studies: general methodology and example of application to ferroic perovskite oxides, J. Phys.: Condens. Matter **25**, 305401 (2013).

[14] C. Escorihuela-Sayalero, J. C. Wojdeł, and J. Íñiguez, Efficient systematic scheme to construct second-principles lattice dynamical models, Phys. Rev. B **95**, 094115 (2017).

[15] M. Graf and J. Íñiguez, A unified perturbative approach to electrocaloric effects, Commun. Mater. **2**, 60 (2021).

[16] L. Bastogne, F. Gómez-Ortiz, S. Anand, and P. Ghosez, Dynamical manipulation of polar topologies from acoustic phonon excitations, Nano Lett. **24**, 13783 (2024).

[17] D. E. Murillo-Navarro, M. Graf, and J. Íñiguez, Coexisting conventional and inverse mechanocaloric effects in ferroelectrics, Phys. Rev. B **104**, 184112 (2021).

[18] J. Zhang, L. Bastogne, X. He, G. Tang, Y. Zhang, P. Ghosez, and J. Wang, Structural phase transitions and dielectric properties of $BaTiO_3$ from a second-principles method, Phys. Rev. B **108**, 134117 (2023).

[19] F. Gómez-Ortiz, L. Bastogne, S. Anand, M. Yu, X. He, and P. Ghosez, Switchable skyrmion-antiskyrmion tubes in rhombohedral $BaTiO_3$ and related materials, Phys. Rev. B **111**, L180104 (2025).

[20] F. Gómez-Ortiz, L. Bastogne, X. He, and P. Ghosez, Precise control and displacement of polar textures from inhomogeneous and time-dependent electric fields, Phys. Rev. B **111**, 134107 (2025).

[21] X. Gonze, B. Amadon, G. Antonius, F. Arnardi, L. Baguet, J.-M. Beuken, J. Bieder, F. Bottin, J. Bouchet, E. Bousquet

et al., The ABINIT project: Impact, environment and recent developments, Comput. Phys. Commun. **248**, 107042 (2020).

[22] M. J. Verstraete, J. Abreu, G. E. Allemand, B. Amadon, G. Antonius, M. Azizi, L. Baguet, C. Barat, L. Bastogne, R. Bejaud *et al.*, ABINIT 2025: New capabilities for the predictive modeling of solids and nanomaterials, arXiv:2507.08578.

[23] D. R. Hamann, Optimized norm-conserving Vanderbilt pseudopotentials, Phys. Rev. B **88**, 085117 (2013).

[24] M. J. Van Setten, M. Giantomassi, E. Bousquet, M. J. Verstraete, D. R. Hamann, X. Gonze, and G.-M. Rignanese, The PSEUDODOJO: Training and grading a 85 element optimized norm-conserving pseudopotential table, Comput. Phys. Commun. **226**, 39 (2018).

[25] H. J. Monkhorst and J. D. Pack, Special points for Brillouin-zone integrations, Phys. Rev. B **13**, 5188 (1976).

[26] X. Gonze and C. Lee, Dynamical matrices, born effective charges, dielectric permittivity tensors, and interatomic force constants from density-functional perturbation theory, Phys. Rev. B **55**, 10355 (1997).

[27] L. Bastogne, J. Bieder, A. Martin, M. Schmitt, A. Sasani, H. Zhang, F. Gómez-Ortiz, S. Bandyopadhyay, X. He, and P. Ghosez, MULTIBINIT: Toward automatized second-principles models – lattice part (unpublished).

[28] S. Duane, A. D. Kennedy, B. J. Pendleton, and D. Roweth, Hybrid Monte Carlo, Phys. Lett. B **195**, 216 (1987).

[29] M. Betancourt, A conceptual introduction to Hamiltonian Monte Carlo, arXiv:1701.02434.

[30] G. Henkelman and H. Jónsson, Improved tangent estimate in the nudged elastic band method for finding minimum energy paths and saddle points, J. Chem. Phys. **113**, 9978 (2000).

[31] D. Sheppard, R. Terrell, and G. Henkelman, Optimization methods for finding minimum energy paths, J. Chem. Phys. **128**, 134106 (2008).

[32] F. Knoop, N. Shulumba, A. Castellano, J. P. Alvarinhas Batista, R. Farris, M. J. Verstraete, M. Heine, D. Broido, D. S. Kim, J. Klarbring *et al.*, TDEP: Temperature dependent effective potentials, J. Open Source Softw. **9**, 6150 (2024).

[33] E. Zatterin, P. Ondrejkovic, L. Bastogne, C. Lichtensteiger, L. Tovaglieri, D. A. Chaney, A. Sasani, T. Schülli, A. Bosak, S. Leake, P. Zubko, P. Ghosez, J. Hlinka, J.-M. Triscone, and M. Hadjimichael, Assessing the ubiquity of Bloch domain walls in ferroelectric lead titanate superlattices, Phys. Rev. X **14**, 041052 (2024).

[52] S. Chege, L. Bastogne, F. Gómez-Ortiz, J. Sifuna, G. Amolo, P. Ghosez, and J. Junquera, Strain dependence of the Bloch domain component in 180° domains in bulk PbTiO₃ from first-principles, J. Appl. Phys. **138**, 044105 (2025).

[34] H. Zhang, H.-C. Thong, L. Bastogne, C. Gui, X. He, and P. Ghosez, Finite-temperature properties of antiferroelectric perovskite PbZrO₃ from deep learning interatomic potential, Phys. Rev. B **110**, 054109 (2024).

[35] H. Sharma, J. Kreisel, and P. Ghosez, First-principles study of PbTiO₃ under uniaxial strains and stresses, Phys. Rev. B **90**, 214102 (2014).

[36] M. Zacharias and F. Giustino, One-shot calculation of temperature-dependent optical spectra and phonon-induced band-gap renormalization, Phys. Rev. B **94**, 075125 (2016).

[37] L. Bastogne and P. Ghosez, PbTiO₃ second-principles interatomic potential (2025), https://doi.org/10.58119/ULG/EW3NNJ.

[38] S. Liu, I. Grinberg, H. Takenaka, and A. M. Rappe, Reinterpretation of the bond-valence model with bond-order formalism: An improved bond-valence-based interatomic potential for PbTiO3, Phys. Rev. B **88**, 104102 (2013).

[39] J. Wu, J. Yang, L. Ma, L. Zhang, and S. Liu, Modular development of deep potential for complex solid solutions, Phys. Rev. B **107**, 144102 (2023).

[40] M. Dawber, N. Stucki, C. Lichtensteiger, S. Gariglio, P. Ghosez, and J.-M. Triscone, Tailoring the properties of artificially layered ferroelectric superlattices, Adv. Mater. **19**, 4153 (2007).

[41] J.-T. Wang, K. Bu, F. Hu, J. Wang, and C. Chen, Finite-temperature properties of PbTiO₃ by molecular dynamics simulations, J. Appl. Phys. **134**, 214101 (2023).

[42] S. F. Yuk, K. C. Pitike, S. M. Nakhmanson, M. Eisenbach, Y. W. Li, and V. R. Cooper, Towards an accurate description of perovskite ferroelectrics: Exchange and correlation effects, Sci. Rep. **7**, 43482 (2017).

[43] W. Zhong, D. Vanderbilt, and K. M. Rabe, First-principles theory of ferroelectric phase transitions for perovskites: The case of BaTiO₃, Phys. Rev. B **52**, 6301 (1995).

[44] Y. Qi, S. Liu, I. Grinberg, and A. M. Rappe, Atomistic description for temperature-driven phase transitions in BaTiO₃, Phys. Rev. B **94**, 134308 (2016).

[45] L. Gigli, M. Veit, M. Kotiuga, G. Pizzi, N. Marzari, and M. Ceriotti, Thermodynamics and dielectric response of BaTiO₃ by data-driven modeling, npj Comput. Mater. **8**, 209 (2022).

[46] P. Xie, Y. Chen, W. E., and R. Car, Thermal disorder and phonon softening in the ferroelectric phase transition of lead titanate, Phys. Rev. B **111**, 094113 (2025).

[47] G. Shirane, J. Axe, J. Harada, and J. Remeika, Soft ferroelectric modes in lead titanate, Phys. Rev. B **2**, 155 (1970).

[48] W. Cochran, Crystal stability and the theory of ferroelectricity, Phys. Rev. Lett. **3**, 412 (1959).

[49] I. Tomeno, Y. Ishii, Y. Tsunoda, and K. Oka, Lattice dynamics of tetragonal PbTiO₃, Phys. Rev. B **73**, 064116 (2006).

[50] M. Fontana, H. Idrissi, G. Kugel, and K. Wojcik, Raman spectrum in PbTiO₃ re-examined: Dynamics of the soft phonon and the central peak, J. Phys.: Condens. Matter **3**, 8695 (1991).

[51] S. Pöykkö and D. Chadi, *Ab initio* study of 180 domain wall energy and structure in PbTiO₃, Appl. Phys. Lett. **75**, 2830 (1999).

[53] Y. Gu, M. Li, A. N. Morozovska, Y. Wang, E. A. Eliseev, V. Gopalan, and L.-Q. Chen, Flexoelectricity and ferroelectric domain wall structures: Phase-field modeling and DFT calculations, Phys. Rev. B **89**, 174111 (2014).

[54] Y. J. Wang, D. Chen, Y. L. Tang, Y. L. Zhu, and X. L. Ma, Origin of the Bloch-type polarization components at the 180° domain walls in ferroelectric PbTiO₃, J. Appl. Phys. **116**, 224105 (2014).

[55] X. Ma, H. Chen, R. He, Z. Yu, S. Prokhorenko, Z. Wen, Z. Zhong, J. Íñiguez-González, L. Bellaiche, D. Wu *et al.*, Active learning of effective Hamiltonian for super-large-scale atomic structures, npj Comput. Mater. **11**, 70 (2025).

[56] Y. T. Chen, Y. L. Tang, Y. L. Zhu, Y. J. Wang, M. J. Han, M. J. Zou, Y. P. Feng, W. R. Geng, F. H. Gong, and X. L. Ma, Periodic vortex-antivortex pairs in tensile strained PbTiO₃ films, Appl. Phys. Lett. **117**, 192901 (2020).

[57] F. Di Rino, M. Sepliarsky, and M. G. Stachiotti, Topology of the polarization field in PbTiO₃ nanoparticles of different

shapes by atomic-level simulations, J. Appl. Phys. **127**, 144101 (2020).

[58] L. He and D. Vanderbilt, First-principles study of oxygen-vacancy pinning of domain walls in $PbTiO_3$, Phys. Rev. B **68**, 134103 (2003).

[59] V. Stepkova, P. Marton, and J. Hlinka, Ising lines: Natural topological defects within ferroelectric Bloch walls, Phys. Rev. B **92**, 094106 (2015).

[60] V. Stepkova and J. Hlinka, On the possible internal structure of the ferroelectric Ising lines in $BaTiO_3$, Phase Trans. **90**, 11 (2017).

[61] S. Cherifi-Hertel, H. Bulou, R. Hertel, G. Taupier, K. D. Dorkenoo, C. Andreas, J. Guyonnet, I. Gaponenko, K. Gallo, and P. Paruch, Non-Ising and chiral ferroelectric domain walls revealed by nonlinear optical microscopy, Nat. Commun. **8**, 15768 (2017).

[62] S. Liu, I. Grinberg, and A. M. Rappe, Intrinsic ferroelectric switching from first principles, Nature (London) **534**, 360 (2016).

[63] A. Bogdanov and A. Hubert, The stability of vortex-like structures in uniaxial ferromagnets, J. Magn. Magn. Mater. **195**, 182 (1999).

[64] J. Hagemeister, A. Siemens, L. Rózsa, E. Y. Vedmedenko, and R. Wiesendanger, Controlled creation and stability of $k\pi$ skyrmions on a discrete lattice, Phys. Rev. B **97**, 174436 (2018).

[65] R. Streubel, L. Han, M.-Y. Im, F. Kronast, U. K. Rößler, F. Radu, R. Abrudan, G. Lin, O. G. Schmidt, P. Fischer *et al.*, Manipulating topological states by imprinting non-collinear spin textures, Sci. Rep. **5**, 8787 (2015).

[66] B. Göbel, I. Mertig, and O. A. Tretiakov, Beyond skyrmions: Review and perspectives of alternative magnetic quasiparticles, Phys. Rep. **895**, 1 (2021).

[67] A. G. Kolesnikov, M. E. Stebliy, A. S. Samardak, and A. V. Ognev, Skyrmionium–high velocity without the skyrmion Hall effect, Sci. Rep. **8**, 16966 (2018).

[68] F. Zheng, H. Li, S. Wang, D. Song, C. Jin, W. Wei, A. Kovács, J. Zang, M. Tian, Y. Zhang *et al.*, Direct imaging of a zero-field target skyrmion and its polarity switch in a chiral magnetic nanodisk, Phys. Rev. Lett. **119**, 197205 (2017).

[69] D. Foster, C. Kind, P. J. Ackerman, J.-S. B. Tai, M. R. Dennis, and I. I. Smalyukh, Two-dimensional skyrmion bags in liquid crystals and ferromagnets, Nat. Phys. **15**, 655 (2019).

[70] K. Kasai, T. Nojima, Y. Wang, T. Xu, H. Hirakata, and T. Shimada, Mechanical writing of polar skyrmionic topological states via extrinsic Dzyaloshinskii-Moriya-like flexoelectricity in ferroelectric thin films, ACS Nano **18**, 32451 (2024).

[71] T. Linker, K.-i. Nomura, S. Fukushima, R. K. Kalia, A. Krishnamoorthy, A. Nakano, K. Shimamura, F. Shimojo, and P. Vashishta, Squishing skyrmions: Symmetry-guided dynamic transformation of polar topologies under compression, J. Phys. Chem. Lett. **13**, 11335 (2022).

[72] J. Milnor, *Topology from the Differentiable Viewpoint* (The University Press of Virginia, Charlottesville, 1965).